

High-fidelity software-defined quantum logic on a superconducting qudit

Xian Wu,* S. L. Tomarken, N. Anders Petersson, L. A. Martinez, Yaniv J. Rosen, and Jonathan L DuBois
Lawrence Livermore National Laboratory, Livermore, CA 94550, USA

(Dated: July 22, 2022)

We present an efficient approach to achieving arbitrary, high-fidelity control of a multi-level quantum system using optimal control techniques. As an demonstration, we implement a continuous, software-defined microwave pulse to realize a $0 \leftrightarrow 2$ SWAP gate that achieves an average gate fidelity of 99.4%. We describe our procedure for extracting the system Hamiltonian, calibrating the quantum and classical hardware chain, and evaluating the gate fidelity. Our work represents an alternative, fully generalizable route towards achieving universal quantum control by leveraging optimal control techniques.

Due to recent breakthroughs in quantum technology [1–7], quantum information is entering the Noisy Intermediate-Scale Quantum (NISQ) era [8]. In the NISQ era, quantum processors consisting of 50-100 qubits and lacking fault-tolerant noise correction protocols have the potential to perform tasks surpassing today’s best classical computers [4, 9, 10]. Most recent efforts to reduce computational error rates have focused on extending qubit coherence times by leveraging improvements in fabrication and qubit design, e.g. Refs. 11–13. However, a less explored route lies in harnessing classical computing power to co-design efficient quantum control protocols in order to extend the computational limits of state-of-the-art quantum processors [14–16]. One promising avenue in this direction is quantum optimal control [14, 17, 18], where nonlinear optimization techniques are utilized to design microwave pulses that can perform arbitrary unitary operations. This allows for a departure from traditional discrete gate-set approaches where quantum states are controlled using a reduced set of ‘primitive’ single- and two-qubit gates.

In the NISQ era, one of the most anticipated applications of quantum computation is quantum simulation [19], which often requires continuous control over complex multi-qubit time-evolution. Currently, reduced gate-set fidelities $\geq 99\%$ are routinely achieved for single-qubit gates [5, 20–22] and, more recently, for several two-qubit gates as well [2, 21, 23–26]. However, standard fixed gate-set approaches tend to perform poorly for quantum simulation because the desired complex quantum system evolution can only be achieved by concatenating large numbers of primitive gates, resulting in very deep quantum circuits with cumulative error rates that are often substantially worse than the constituent primitive gate errors [27–30]. In contrast with reduced gate-set approaches, employing quantum optimal control methods allows one, in principle, to construct a single custom many-body gate that realizes a requested target evolution directly. Complex gates constructed with the aid of

optimal control algorithms often require net shorter durations and potentially yield higher process fidelities than is possible with composite gate sequences [16, 31]. Before one can implement an optimal control gate, the device and control Hamiltonian must be understood in detail and successfully mapped to the target Hamiltonian. This requires a detailed characterization of not just the physical quantum hardware but also the quantum-classical transfer function arising from room temperature electronics, cryogenic control lines, and related components. Once the device Hamiltonian and transfer function are known, no gate-level hardware calibration is required for the application of arbitrary optimal control gates, making this approach highly flexible.

In this work, we report our experimental effort towards implementing quantum optimal control on a superconducting transmon qudit to realize a nontrivial unitary operator. By extending the dimension of the Hilbert space to a d -level *qudit*, we achieve a computational advantage with fewer physical devices [1, 32–35]. Previous studies on multi-level transmon qudits indicate that the higher energy levels are a potentially useful quantum resource [36–39]. In this manuscript, we present full characterization of the lowest four energy levels of a three-dimensional (3D) transmon device [40] and the linear quantum-classical transfer function that underlie the calculation of the optimal control gate. We perform both single-gate and repeated-gate measurements. Our data show good agreement with master equation simulations of the qudit response to the optimized control pulse solution. We demonstrate an efficient characterization of the process matrix and estimate an average gate fidelity of 99.4%.

The system’s Hamiltonian in the presence of time-dependent control drives is given by $H(t) = H_0 + \sum_{j=1}^N u_j(t)H_j$ where H_0 describes the time-independent Hamiltonian and the H_j are the available control Hamiltonians. The $u_j(t)$ are time varying amplitudes for each specific control. In a closed quantum system, the dynamics are governed only by the Schrödinger equation. Using numerical optimization [14, 41] we can find a set of $u_j(t)$ that realize the target unitary transformation U_{targ} ,

* Correspondence to: wu47@llnl.gov

within an acceptable error, according to

$$U_{\text{targ}} = \mathcal{T} e^{-i \int_0^{T_g} H(t) dt / \hbar}, \quad (1)$$

where \mathcal{T} represents time-ordering of the exponential, T_g is the gate time, and \hbar is Planck's reduced constant.

For the purposes of demonstrating the optimal control technique, we have chosen a $0 \leftrightarrow 2$ SWAP gate as the U_{targ} . The first three levels $|0\rangle, |1\rangle, |2\rangle$ of our transmon qudit make up the computational space while the fourth level $|3\rangle$ monitors the leakage from the computational space to higher energy levels. The transmon is coupled to a 3D aluminum superconducting cavity which is used to dispersively read out the qudit state [42]. The experimental setup for demonstrating the optimal control approach is shown in Fig. 1. Parameters of the transmon and cavity are listed in Table I. The transmon's Hamiltonian is time-independent so that H_0 is given by $H_0 = \hbar \sum_{k=0}^3 \omega_k |k\rangle \langle k|$ where $\hbar \omega_k$ and $|k\rangle$ are the eigenenergy and eigenstate of the transmon's k th level. We set $\hbar = 1$ for further equations in this manuscript. Because the optimized control pulse must drive qudit transitions at roughly 4 GHz, the dominant frequency components of the control pulse will be about 3 GHz or more detuned from the readout cavity. As a result, in both the drive Hamiltonian and interaction Hamiltonian (below), we can safely neglect terms associated with the readout cavity.

Next, we derive the control Hamiltonian H_j for the qudit being driven by a microwave pulse. The time-dependent Hamiltonian that describes the interaction between the electric field inside the cavity and a multi-level quantum system is [43]

$$\begin{aligned} H_{\text{int}} &= \sum_{j=1}^N u_j H_j = (c + c^\dagger)(\xi e^{-i\omega_d t} + \xi^* e^{i\omega_d t}) \\ &= (c + c^\dagger)(2 \text{Re}(\xi) \cos(\omega_d t) + 2 \text{Im}(\xi) \sin(\omega_d t)) \end{aligned} \quad (2)$$

where c (c^\dagger) is the lowering (raising) operator in the transmon eigenbasis, ξ is the drive strength, and ω_d is the drive frequency.

To slow down the time scales in the numerical optimization, we transform into the rotating frame of the drive using the unitary operator

$$R(t) = \exp([i\omega_d t (\sum_k k |k\rangle \langle k|)]) \text{ yielding}$$

$$\begin{aligned} H_{\text{rot}} &= R(t) (H_0 + H_{\text{int}}) R(t)^\dagger - iR(t) \dot{R}(t)^\dagger \\ &= \sum_k \Delta_k |k\rangle \langle k| + \text{Re}(\xi) (\tilde{c} + \tilde{c}^\dagger) - i \text{Im}(\xi) (\tilde{c} - \tilde{c}^\dagger) \end{aligned} \quad (3)$$

where $\Delta_k \equiv \omega_k - k\omega_d$, and \tilde{c} (\tilde{c}^\dagger) is the lowering (raising) operator in the rotating frame. We set $\omega_0 = 0$, choose $\omega_d = \omega_1$, and make use of the rotating wave approximation wherein terms oscillating at $\pm(\omega_k + k\omega_d)$ are neglected. In the rotating frame we have two H_j and two u_j to be optimized:

$$\begin{aligned} H_1 &= \tilde{c} + \tilde{c}^\dagger & H_2 &= -i(\tilde{c} - \tilde{c}^\dagger) \\ u_1 &= \text{Re}(\xi) & u_2 &= \text{Im}(\xi). \end{aligned} \quad (4)$$

As shown in Eq. 4, the time-dependence on the control functions u_1, u_2 has been relieved. Because we have chosen to optimize the control pulse in the rotating frame, the target operator will transform according to $R(T_g) U_{\text{targ}} R^\dagger(0)$.

The device Hamiltonian H_0 is constructed manually from the measured qudit transition frequencies listed in Table. I. In order to extract the transmon's raising and lower operators, we model the transmon as a Cooper pair box in the charge basis and explicitly calculate the raising and lowering operators for a truncated charge basis. See the Supplemental Material (SM) for details of the model and calculation.

TABLE I. Device parameters

Parameter	Value
$ 0\rangle - 1\rangle$ transition frequency $\omega_q^{(0,1)}/2\pi$	4.09948 GHz
Relaxation time T_1 for the $ 0\rangle - 1\rangle$ transition	55 μs
Ramsey decay time T_2^* for the $ 0\rangle - 1\rangle$ transition	35 μs
$ 1\rangle - 2\rangle$ transition frequency $\omega_q^{(1,2)}/2\pi$	3.87409 GHz
Relaxation time T_1 for the $ 1\rangle - 2\rangle$ transition	26 μs
Echo time T_2^E for the $ 1\rangle - 2\rangle$ transition	13 μs
$ 2\rangle - 3\rangle$ transition frequency $\omega_q^{(2,3)}/2\pi$	3.61938 GHz
Relaxation time T_1 for the $ 2\rangle - 3\rangle$ transition	18 μs
Echo time T_2^E for the $ 2\rangle - 3\rangle$ transition	7.5 μs
Readout resonator frequency $\omega_r/2\pi$	7.0768 GHz
Effective dispersive coupling strength, $\chi_{qc}/2\pi$	1.017 MHz

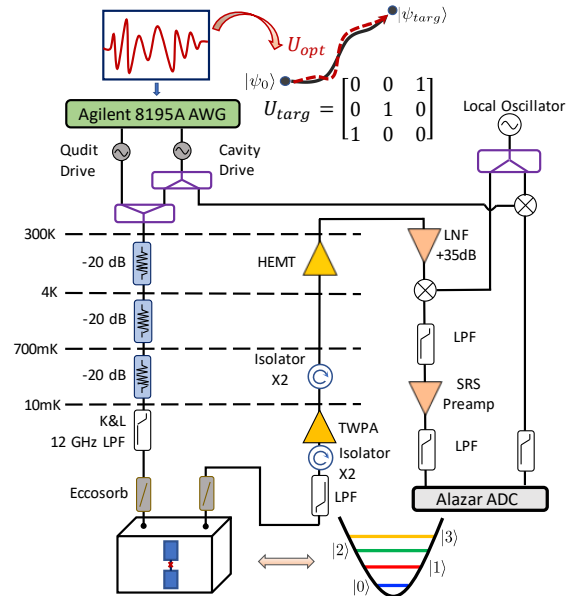


FIG. 1. **Experiment setup for implementing an optimized control pulse on a transmon qudit.** The top cartoon illustrates the optimization procedure for a qudit control pulse given a target unitary operator. The lower schematic depicts the measurement diagram. The qudit is implemented using a 3D transmon.

Now, we turn to the numerical optimization. There are currently multiple software packages available for finding optimal control pulses [44, 45]. Most implementations rely on gradient-descent methods [14, 46] where the continuous gate can be subjected to experimentally relevant constraints such as maximal drive amplitude and gradient as well as boundary conditions of the control pulse. Here, we use the recently developed package described in Ref. 47 because it gives precise control over the dominant frequencies in the spectra of the control functions. The optimizer minimizes the objective function \mathcal{G} defined as below:

$$\mathcal{G} = (1 - F_g^2) + \frac{1}{T_g} \int_0^{T_g} \text{Tr} \left(U_{\text{opt}}^\dagger(t) W U_{\text{opt}}(t) \right) dt \quad (5)$$

$$F_g = \frac{1}{d} \left| \text{Tr} \left(U_{\text{targ}}^\dagger U_{\text{opt}}(T_g) \right) \right|, \quad W = \begin{pmatrix} 0 & & \\ & 0 & \\ & & 0 \end{pmatrix}$$

where U_{targ} is the target unitary operator in the rotating frame. $U_{\text{opt}}(t)$ is the propagator based on the time-dependent control solution and is used to calculate the gate fidelity F_g for the generated control solution. The second term in Eq. 5 calculates the $|3\rangle$ population throughout the gate which is used to minimize the leakage outside the computational space.

T_g is chosen to be 150 ns to comply with the maximum drive amplitude we can apply in our measurement setup. Figure 1 contains the measurement circuit details. A Keysight 8195A arbitrary waveform generator (AWG) directly synthesizes the control drive with an output limit of 1 V. Taking into account the total attenuation of the input line, the drive strength is limited to about 6 MHz in the rotating frame (or 12 MHz in the laboratory frame). T_g may be further reduced by decreasing the line attenuation, increasing the AWG output limit, or reducing the coupling quality factor for signals entering the qudit cavity. See the SM for details on the experimental setup. We set the time resolution of the control pulse to 1/32 ns to match the 32 GSa/s sampling rate of the AWG. Figure S2(b) in the SM shows the optimized control functions in both the rotating and laboratory frames with calculated $F_g = 99.997\%$.

In order to investigate the $0 \leftrightarrow 2$ SWAP gate, we perform both single- and repeated-gate measurements. First, we characterize the behavior of a single gate by measuring the state occupation probabilities for the lowest four qudit states throughout the duration of the gate. We initialize the qudit state separately to $|0\rangle, |1\rangle, |2\rangle, |3\rangle$ and measure the occupation probability for each state at 1 ns intervals as shown in Fig. 2(a)–(d). We perform single-shot readout at the end of each measurement and infer the final state of the qudit through classification (see SM for details). In order to evaluate the performance of a single gate, we simulate the qudit dynamics using the Lindblad master equation formalism with the QuTiP python library [44]. Because the total gate time

is much shorter than the coherence times of all of the states involved, Lindbladian terms [48] associated with relaxation and dephasing are not included in the simulations shown as solid lines in Fig. 2. We observe good agreement between our measurements and simulations.

The qudit probability evolution tracks the dominant frequency modes of the control signal throughout the duration of the pulse and can be used to study the dynamics of the control pulse which often contains a broad mixture of frequency components and is difficult to intuit in the time-domain directly. Whenever occupation between adjacent states $|i\rangle$ and $|i+1\rangle$ is exchanged, the frequency component at $f_q^{(i,i+1)} = \omega_q^{(i,i+1)}/2\pi$ of the drive has significant amplitude. For example, population exchange between states $|0\rangle$ and $|1\rangle$ at the beginning of the control pulse in Fig. 2(a) and (b) indicates a strong spectral contribution from $f_q^{(0,1)} = \omega_q^{(0,1)}/2\pi$ until about 40 ns where a small plateau of $|0\rangle$ develops. Later, the $f_q^{(0,1)}$ drive is resumed with stronger intensity until about 120 ns, after which the $|0\rangle$ population becomes essentially flat. A similar analysis applies to the $f_q^{(1,2)}$ Fourier component and the $|1\rangle$ and $|2\rangle$ state occupation in Fig. 2(b) and (c). Importantly, Fig. 2(d) verifies that there is no drive component near frequency $f_q^{(2,3)}$. Our qudit analysis of the control pulse is consistent with time-frequency analysis of the control pulse. Morlet wavelet analysis with 150 cycles [49] of the control signal is presented in Fig. 2(e) and (f) and verifies that the dominant frequency components are centered around $f_q^{(0,1)}$ and $f_q^{(1,2)}$ and that their amplitudes vary in time in agreement with the qudit population trajectories in Fig. 2(a)–(d).

Finally, we analyze the gate performance by measuring the qudit state occupation upon repeated application of the optimal control gate up to 21 times. Measurements are performed for all four initial states with results presented in Fig. 3(a)–(d). For initial states $|0\rangle$ and $|2\rangle$, coherent state population exchange between $|0\rangle$ and $|2\rangle$ is observed. There is significant leakage into $|1\rangle$, while leakage into $|3\rangle$ is minimal. For the initial states $|1\rangle$ and $|3\rangle$, no obvious coherent behavior is observed, as expected for a $0 \leftrightarrow 2$ SWAP gate. As the number of gate applications increases, the amplitude of the $|0\rangle$ and $|2\rangle$ population transfer decreases, an effect that we attribute to both relaxation and decoherence intrinsic to the physical device and control errors (imperfect implementation of the control pulse). Additionally, there are errors associated with state preparation and state readout, however, we believe these latter contributions are much less significant due to the successful single-gate measurements presented in Fig. 2.

To examine the device's intrinsic error rate, we simulate the qudit response under repeated applications of the control pulse with the realistic T_1 and T_2 errors listed in Table I. The simulation result is plotted in Fig. S2(a)–(d) of the SM and qualitatively agrees with our measure-

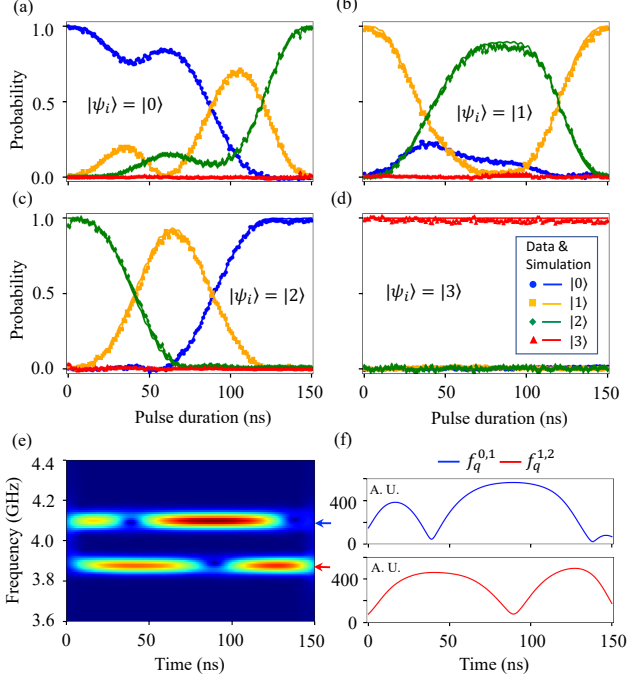


FIG. 2. Measuring the qudit state probabilities during a single gate application and time-frequency analysis of the control pulse (a)–(d) Initial states are prepared in $|0\rangle, |1\rangle, |2\rangle, |3\rangle$ for each gate application. Each data point in (a) contains 2048 single shot measurements. Each data point in (b)–(d) contains 3072 single shot measurements. $|1\rangle$ is prepared with a square pulse at $\omega_q^{(0,1)}$. $|2\rangle$ and $|3\rangle$ are prepared with a sequence of square pulse at $\omega_q^{(0,1)}, \omega_q^{(1,2)}$ and $\omega_q^{(2,3)}$. Solid lines are simulation results for ideal gate implementation. (e) Wavelet transformation of the laboratory frame control pulse. (f) Linecuts of (e) at $f_q^{(0,1)}$ and $f_q^{(1,2)}$.

ment results. The simulation for the $|3\rangle$ state is in good agreement, suggesting our estimation of the device's intrinsic error is accurate. The simulations of the states driven by the control pulse show less attenuation of the $|0\rangle$ and $|2\rangle$ population transfer and less leakage into the $|1\rangle$ state, suggesting that errors associated with application of the control drive contribute significantly to the total error rate. Based on the measurement outcome of the computational space, we extract the process matrix χ to describe the drive's effect on an arbitrary input state ρ . Following Ref. 50, we can choose one complete gate set to describe any process for a d -dimensional system:

$$\mathcal{E}(\rho) = \sum_{m,n=0}^{d^2-1} \chi_{mn} B_m \rho B_n^\dagger \quad (6)$$

$$B_n = \{I, Z_{01}, Z_{12}, X_{01}, X_{12}, Y_{01}, Y_{12}, X_{01}X_{12}, X_{12}X_{01}\}. \quad (7)$$

Here, $\{B_n\}$ forms a complete gate set to represent any $d \times d$ matrix. χ is a positive superoperator which com-

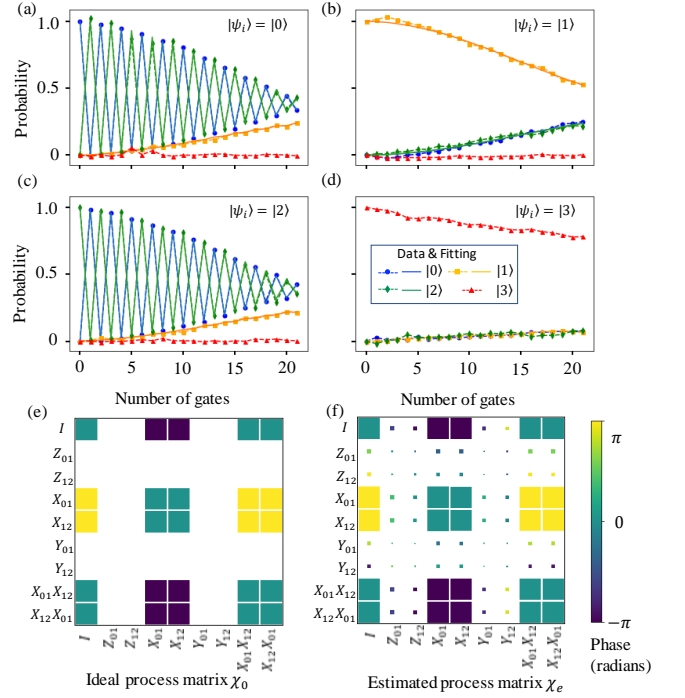


FIG. 3. Measurement of state evolution during repeated gate application and process matrix analysis (a)–(d) Measured state probabilities for multiple gate applications when preparing the initial state in $|0\rangle, |1\rangle, |2\rangle, |3\rangle$. Symbols connected with dashed lines are measurement results and each data point contains 20480 records. Solid lines are simulations of the expected measurement outcome with the estimated process matrix. (e),(f) Hinton diagrams of the ideal process matrix and estimated process matrix for the implemented $0 \leftrightarrow 2$ SWAP gate. The magnitude and phase for each matrix element are represented by its area and color, respectively.

pletely characterizes the process \mathcal{E} using the basis operators $\{B_n\}$. The established procedure [51] to estimate the process matrix χ is to prepare many different initial states, apply the mapping once, and fit for the most likely χ based on the measurement outcomes. Here, we perform the estimation of χ using a different method. We prepare three initial states $|0\rangle, |1\rangle, |2\rangle$ and apply the mapping sequentially to obtain a series of state occupation probabilities. The best-fit χ matrix is estimated by minimizing the difference between the generated state probabilities for a given implementation of χ and the measurement results. We are motivated to use this method because quantum simulation often requires repeated application of the same gate [16, 28], from which the process fidelity can be estimated without further experiments. The caveat of this approach is that there is no guarantee that the set of generated states is sufficient to constrain the fitting.

We examine the measured state populations in Fig. 3(a)–(c). We observe that states spanning a variety of basis elements are generated. This indicates we have

likely generated a sufficient number of states to constrain the fit results. We believe that all states remain highly coherent because the measurement outcome is produced mainly by the gate error (as opposed to state decay or dephasing). The ideal and estimated χ matrices are plotted in Fig. 3(e) and (f) for comparison. Following Ref. 50, we calculate entanglement and gate fidelity according to equations below:

$$F_e(\rho, U, \mathcal{E}) = \sum_{mn} \chi_{e,mn} \text{Tr}(U^\dagger B_m \rho) \text{Tr}(\rho B_n^\dagger U) \quad (8)$$

$$F_g(|\psi\rangle, U, \mathcal{E}) = \langle\psi| U^\dagger \mathcal{E}(|\psi\rangle\langle\psi|) U |\psi\rangle \quad (9)$$

where χ_e is the estimated process matrix, ρ represents the density matrix form of the input state, and $|\psi\rangle$ represents a pure state. The averaged entanglement fidelity is 99.2% and the averaged gate fidelity is 99.4%.

Several aspects of our optimal control scheme can be improved to further reduce the gate error. The accuracy and resolution of our current spectral filter can be improved by using a multi-state Rabi model to predict the drive strength for each frequency component (see the SM for details). Additionally, we have observed that the AWG itself has a significant nonlinear output as a function of the drive amplitude. Careful characterization of the AWG output and applying appropriate compensation in software would guarantee more faithful implementation of the intended control waveform. Increasing the qudit drive coupling strength can reduce the error arising from qudit decoherence by allowing a shorter total gate time.

We have demonstrated a $0 \leftrightarrow 2$ SWAP gate with a software-defined optimal control pulse on the lowest four levels of a 3D transmon qudit. In stark contrast with conventional primitive gate sets, which must be carefully optimized depending on the total duration and circuit-depth of the target gate, our optimal control solution requires no gate-level tuning once the device Hamiltonian and spectral transfer function of the measurement chain are known. Moreover, because the device Hamiltonian and transfer function are stable over time, we can implement additional optimal control gates without further hardware calibration (e.g. Ref. 31). Our results show that gate fidelities $>99\%$ can be achieved with pulses generated with an optimal control algorithm, reaching a similar benchmark as discrete gate-set implementations. This proof of principle demonstration can be easily generalized to arbitrary unitary transformations, offering an alternate route to achieving high-fidelity quantum control. Additionally, these optimal control techniques can be used in concert with discrete gate-set approaches to optimize the pulse shape of the constituent gates [52]. Our results provide a guidepost for further development of optimal control techniques for many quantum information applications, particularly in the NISQ era.

This work was performed under the auspices of the

U.S. Department of Energy by Lawrence Livermore National Laboratory under Contract DE-AC52-07NA27344. The authors gratefully acknowledge support from the Department of Energy Office of Advanced Scientific Computing Research, Quantum Testbed Pathfinder Program under Award 2017-LLNL-SCW1631, the National Nuclear Security Administration Advanced Simulation and Computing Beyond Moores Law program (LLNL-ABS-795437) and Lab Directed Research and Development award LDRD19-DR-005.(LLNL-JRNL-810657-DRAFT)

-
- [1] J. M. Chow, J. M. Gambetta, W. Cross, Andrew, S. T. Merkel, C. Rigetti, and M. Steffen, *New Journal of Physics* **15** (2013).
 - [2] Y. Chen, C. Neill, P. Roushan, N. Leung, M. Fang, R. Barends, J. Kelly, B. Campbell, Z. Chen, B. Chiaro, A. Dunsworth, E. Jeffrey, A. Megrant, J. Y. Mutus, P. J. J. O'Malley, C. M. Quintana, D. Sank, A. Vainsencher, J. Wenner, T. C. White, M. R. Geller, A. N. Cleland, and J. M. Martinis, *Phys. Rev. Lett.* **113**, 220502 (2014).
 - [3] J. Kelly, R. Barends, A. G. Fowler, A. Megrant, E. Jeffrey, T. C. White, D. Sank, J. Y. Mutus, B. Campbell, Y. Chen, Z. Chen, B. Chiaro, A. Dunsworth, I. C. Hoi, C. Neill, P. J. J. O'Malley, C. Quintana, P. Roushan, A. Vainsencher, J. Wenner, A. N. Cleland, and J. M. Martinis, *Nature* **519**, 66 (2015).
 - [4] F. Arute, K. Arya, R. Babbush, and et. al., *Nature* **574**, 505 (2019).
 - [5] M. Reagor, C. B. Osborn, N. Tezak, A. Staley, G. Prawiroatmodjo, M. Scheer, and et. al., *Science Advances* **4**, eaao3603 (2018).
 - [6] S. Debnath, N. M. Linke, C. Figgatt, K. A. Landsman, K. Wright, and C. Monroe, *Nature* **536**, 63 (2016).
 - [7] K. Wright, K. M. Beck, S. Debnath, J. M. Amini, Y. Nam, N. Grzesiak, J. S. Chen, N. C. Pienti, M. Chmielewski, C. Collins, K. M. Hudek, J. Mizrahi, J. D. Wong-Campos, S. Allen, J. Apisdorf, P. Solomon, M. Williams, A. M. Ducore, A. Blinov, S. M. Kreike-meier, V. Chaplin, M. Keesan, C. Monroe, and J. Kim, *Nature Communications* **10**, 5464 (2019).
 - [8] J. Preskill, *Quantum* **2**, 79 (2018).
 - [9] H. Bernien, S. Schwartz, A. Keesling, H. Levine, A. Omran, H. Pichler, S. Choi, A. S. Zibrov, M. Endres, M. Greiner, V. Vuletić, and M. D. Lukin, *Nature* **551**, 579 (2017).
 - [10] Y. Nam and D. Maslov, *npj Quantum Information* **5**, 44 (2019).
 - [11] A. Nersisyan, S. Poletto, N. Alidoust, R. Manenti, R. Renzas, C. Bui, K. Vu, T. Whyland, Y. Mohan, E. A. Sete, S. Stanwyck, A. Bestwick, and M. Reagor, in *2019 IEEE International Electron Devices Meeting (IEDM)* (2019) pp. 31.1.1–31.1.4.
 - [12] L. Nguyen, B., Y.-H. Lin, A. Somoroff, R. Mencia, Grabon, Nicholas, and V. Manucharyan, E., *Physical Review X* (2019).
 - [13] A. Place, P.M., V. H. L. Rodgers, P. Mundata, and et. al., arXiv: 2003.00024v1 (2020).
 - [14] N. Khaneja, T. Reiss, C. Kehlet, T. Schulte-Herbruggen,

- and J. G. Steffen, J. Magn. Reson. (2005).
- [15] F. F. Floether, P. de Fouquieres, and S. G. Schirmer, New Journal of Physics **14**, 073023 (2012).
 - [16] E. T. Holland, K. A. Wendt, K. Kravvaris, X. Wu, W. Ormand, J. L. DuBois, S. Quaglioni, and F. Pederiva, arXiv:1908.08222v1 (2019).
 - [17] S. Machnes, U. Sander, S. J. Glaser, P. de Fouquieres, A. Gruslys, S. Schirmer, and T. Schulte-Herbrüggen, Phys. Rev. A **84**, 022305 (2011).
 - [18] J. Cheng, H. Deng, and X. Qian, arXiv:2003.00376v1 (2020).
 - [19] G. S. Paraoanu, Journal of Low Temp Phys **175**, 633 (2014).
 - [20] R. Barends, J. Kelly, A. Megrant, A. Veitia, D. Sank, E. Jeffrey, T. C. White, J. Mutus, A. G. Fowler, B. Campbell, Y. Chen, Z. Chen, B. Chiaro, A. Dunswoth, C. Neill, P. O'Malley, P. Roushan, A. Vainsencher, J. Wenner, A. N. Korotkov, A. N. Cleland, and J. M. Martinis, Nature **508**, 500 (2014).
 - [21] S. Sheldon, L. S. Bishop, E. Magesan, S. Filipp, J. M. Chow, and J. M. Gambetta, Phys. Rev. A **93**, 012301 (2016).
 - [22] M. A. Rol, C. C. Bultink, T. E. O'Brien, S. R. de Jong, L. S. Theis, X. Fu, F. Luthi, R. F. L. Vermeulen, J. C. de Sterke, A. Bruno, D. Deurloo, R. N. Schouten, F. K. Wilhelm, and L. DiCarlo, Phys. Rev. Applied **7**, 041001 (2017).
 - [23] A. Dewes, F. R. Ong, V. Schmitt, R. Lauro, N. Boulant, P. Bertet, D. Vion, and D. Esteve, Phys. Rev. Lett. **108**, 057002 (2012).
 - [24] S. Rosenblum, Y. Y. Gao, P. Reinhold, C. Wang, C. J. Axline, L. Frunzio, S. M. Girvin, L. Jiang, M. Mirrahimi, M. H. Devoret, and R. J. Schoelkopf, Nature Communications **9**, 652 (2018).
 - [25] S. S. Hong, A. T. Papageorge, P. Sivarajah, G. Crossman, N. Didier, A. M. Polloreno, E. A. Sete, S. W. Turkowski, M. P. da Silva, and B. R. Johnson, Phys. Rev. A **101**, 012302 (2020).
 - [26] M. Kjaergaard, M. E. Schwartz, A. Greene, G. O. Samach, A. Bengtsson, M. O'Keeffe, C. M. McNally, D. K. Kim, and et. al., arXiv:2001.08838v2 (2020).
 - [27] B. P. Lanyon, C. Hempel, D. Nigg, M. Müller, R. Gerritsma, F. Zähringer, P. Schindler, J. T. Barreiro, M. Rambach, G. Kirchmair, M. Hennrich, P. Zoller, R. Blatt, and C. F. Roos, Science **334**, 57 (2011), <https://science.sciencemag.org/content/334/6052/57.full.pdf>.
 - [28] R. Barends, L. Lamata, J. Kelly, L. Garcia-Alvarez, and A. G. Fowler, Nature Communications **6** (2015).
 - [29] P. J. J. O'Malley, R. Babbush, I. D. Kivlichan, J. Romero, J. R. McClean, R. Barends, J. Kelly, and et. al., Physical Review X (2016).
 - [30] A. Kandala, A. Mezzacapo, K. Temme, M. Takita, M. Brink, J. M. Chow, and J. M. Gambetta, Nature **549**, 242 (2017).
 - [31] Y. Shi, A. R. Castelli, I. Joseph, V. Geyko, F. R. Graziani, S. B. Libby, J. B. Parker, Y. J. Rosen, and J. L. DuBois, arXiv preprint arXiv:2004.06885 (2020).
 - [32] M. Neeley, M. Ansmann, R. C. Bialczak, M. Hofheinz, E. Lucero, A. D. O'Connell, D. Sank, H. Wang, J. Wenner, A. N. Cleland, M. R. Geller, and J. M. Martinis, Science **325**, 722 (2009).
 - [33] B. P. Lanyon, M. Barbieri, M. P. Almeida, T. Jennewein, T. C. Ralph, K. J. Resch, G. J. Pryde, J. L. O'Brien, A. Gilchrist, and A. G. White, Nature Physics **5**, 134 (2009).
 - [34] H. Bechmann-Pasquinucci and A. Peres, Phys. Rev. Lett. **85**, 3313 (2000).
 - [35] N. J. Cerf, M. Bourennane, A. Karlsson, and N. Gisin, Phys. Rev. Lett. **88**, 127902 (2002).
 - [36] R. Bianchetti, S. Filipp, M. Baur, J. M. Fink, C. Lang, L. Steffen, M. Boissonneault, A. Blais, and A. Wallraff, Phys. Rev. Lett. **105**, 223601 (2010).
 - [37] M. J. Peterer, S. J. Bader, X. Jin, F. Yan, A. Kamal, T. J. Gudmundsen, P. J. Leek, T. P. Orlando, W. D. Oliver, and S. Gustavsson, Phys. Rev. Lett. **114**, 010501 (2015).
 - [38] S. Rosenblum, P. Reinhold, M. Mirrahimi, L. Jiang, L. Frunzio, and R. J. Schoelkopf, Science **361**, 266 (2018).
 - [39] M. S. Blok, V. V. Ramasesh, T. Schuster, K. O'Brien, J. M. Kriekbaum, D. Dahlen, A. Morvan, B. Yoshida, N. Y. Yao, and I. Siddiqi, arXiv: 2003.03307v1 (2020).
 - [40] H. Paik, D. I. Schuster, L. S. Bishop, G. Kirchmair, G. Catelani, A. P. Sears, B. R. Johnson, M. J. Reagor, L. Frunzio, L. I. Glazman, S. M. Girvin, M. H. Devoret, and R. J. Schoelkopf, Phys. Rev. Lett. **107**, 240501 (2011).
 - [41] S. Lloyd and S. Montangero, Phys. Rev. Lett. **113**, 010502 (2014).
 - [42] A. Blais, R.-S. Huang, A. Wallraff, S. M. Girvin, and R. J. Schoelkopf, Phys. Rev. A **69**, 062320 (2004).
 - [43] C. Gerry and P. Knight, *Introductory Quantum Optics* (Cambridge University Press, 2004).
 - [44] J. R. Johansson, P. D. Nation, and F. Nori, Computer Physics Communications **184**, 1234 (2013).
 - [45] N. Leung, M. Abdelhafez, J. Koch, and D. Schuster, Phys. Rev. A **95** (2017).
 - [46] P. De Fouquieres, S. Schirmer, S. Glaser, and L. Kuprov, Journal of Magnetic Resonance **212**, 412 (2011).
 - [47] N. A. Petersson, G. M. Fortino, austin E. Copeland, Y. L. Rydin, and J. L. DuBois, arXiv:2001.01013 (2020).
 - [48] L. Goran, Communications in Mathematical Physics **48**, 119 (1976).
 - [49] P. Goupillaud, A. Grossmann, and J. Morlet, Geoploation **23**, 85 (1984).
 - [50] I. L. Chuang and M. A. Nielsen, Journal of Modern Optics **44** (1997).
 - [51] J. M. Chow, J. M. Gambetta, L. Tornberg, J. Koch, L. S. Bishop, A. A. Houck, B. R. Johnson, L. Frunzio, S. M. Girvin, and R. J. Schoelkopf, Phys. Rev. Lett. **102**, 090502 (2009).
 - [52] J. M. Chow, L. DiCarlo, J. M. Gambetta, F. Motzoi, L. Frunzio, S. M. Girvin, and R. J. Schoelkopf, Phys. Rev. A **82**, 040305 (2010).
 - [53] F. Pedregosa, G. Varoquaux, A. Gramfort, V. Michel, B. Thirion, O. Grisel, M. Blondel, P. Prettenhofer, R. Weiss, V. Dubourg, J. Vanderplas, A. Passos, D. Cournapeau, M. Brucher, M. Perrot, and E. Duchesnay, Journal of Machine Learning Research **12**, 2825 (2011).

SUPPLEMENTAL MATERIAL

State classification

The state of the qudit is determined by driving the cavity near its resonance with a square pulse of roughly $3\ \mu\text{s}$ duration and measuring the cavity's state-dependent dispersive shift [42]. Figure S1(a) illustrates the cavity's state-dependent shift $\chi_{qc} \simeq 1.017\ \text{MHz}$. We fix the readout frequency at an optimal point where we obtain the greatest distinguishability in the plane defined by the in-phase (I) and quadrature phase (Q) of the readout signal. In Fig. S1(b), the four separated clusters represent the four lowest qudit states. To collect this data, we first prepared the qudit in one of its lowest four eigenstates with either a single square pulse or a series of square pulses (or thermal relaxation for the ground state) and subsequently measured the signal in $I - Q$ space. Measurements were repeated 51200 times for each initial state. A total of 204800 (I, Q) pairs are used to establish the histogram in Fig. S1(b).

The data in Fig. S1 forms the basis of our qudit state classifier. Specifically, we assume that all data points are generated from a mixture of four Gaussian distributions, each representing one qudit state. We use the GaussianMixture class from the scikit-learn.mixture python module [53] to build the classifier. Based on the $I - Q$ coordinates of the readout signal, the classifier predicts the probability that it belongs to each state. We assign each data point to the state with the highest probability.

Next, we use the classifier to examine each prepared state. The detected state distributions for each prepared state are listed in Table S1. For the prepared state $|0\rangle$, we observe roughly 96% is detected correctly as the $|0\rangle$ state, while 4% is detected as belonging to one of the other four qudit states. We attribute the 4% misclassification error to overlap between the constituent Gaussian distributions of each state. $|1\rangle$ is closest to $|0\rangle$, which

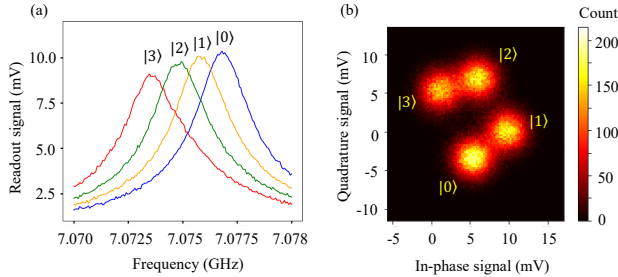


FIG. S1. **Readout of the transmon qudit** (a) State-dependent shifts of the cavity resonance. The cavity shift for adjacent qudit states is approximately $1.017\ \text{MHz}$. (b) Histogram of the in-phase (I) and quadrature phase (Q) signals for the lowest four qudit states.

constitutes most of the 4% difference. For the excited states, state decay during measurement leads to nontrivial populations of the lower energy states. For example, measurements on prepared $|1\rangle$ states show about 8% $|0\rangle$ occupation due mainly to T_1 decay during the $3\ \mu\text{s}$ measurement pulse in addition to misclassification errors due to Gaussian overlap.

In order to best estimate the measured qudit state, we use Table S1 to construct a *confusion matrix* P , which is defined as described in Ref. 5:

$$P = \begin{pmatrix} p(0|0) & p(0|1) & p(0|2) & p(0|3) \\ p(1|0) & p(1|1) & p(1|2) & p(1|3) \\ p(2|0) & p(2|1) & p(2|2) & p(2|3) \\ p(3|0) & p(3|1) & p(3|2) & p(3|3) \end{pmatrix}, \quad (\text{S1})$$

where $p(j|k)$ is defined as the probability of detecting the state $|j\rangle$ given the perfect preparation of the initial state $|k\rangle$.

In this treatment, we describe a given quantum state's probability distribution with a column vector of probabilities \vec{p} . The matrix P relates the detected outcome probability distribution \vec{p}_d and the actual probability distribution \vec{p}_{ac} of the collapsed quantum state as $\vec{p}_d = P\vec{p}_{ac}$. Taking the inverse of the confusion matrix P^{-1} , we can infer the actual qudit probability distribution from the detected probability distribution determined by the classifier. Measurement data shown in Fig. 2 and Fig. 3 of the main text are processed using the methods described above. Due to the instability of the output amplifier at base temperature, the readout signal corresponding to a specific state can itself become unstable over time. This causes a small fraction of our processed data to obtain unphysical probabilities (above 1 or below 0). However, we believe the contribution of the amplifier instability is not significant and the vast majority of the data accurately describes the underlying physics.

Hamiltonian of the qudit

We use the charge basis to describe the transmon Hamiltonian. The effective offset charge n_g is measured in units of the Cooper pair charge $2e$. As usual, the full Hamiltonian consists of the electrostatic component H_{el}

TABLE S1. Distribution of qudit measurement outcomes for different prepared states.

Prepared state	Detected state (%)			
	$ 0\rangle$	$ 1\rangle$	$ 2\rangle$	$ 3\rangle$
$ 0\rangle$	95.85	3.95	0.08	0.12
$ 1\rangle$	8.09	9.09	0.69	0.30
$ 2\rangle$	1.95	19.99	74.08	3.98
$ 3\rangle$	1.84	3.86	17.27	77.03

and the Josephson component H_J :

$$H_T = H_{\text{el}} + H_J \quad (\text{S2})$$

$$H_{\text{el}} = 4E_C (\hat{N} - n_g)^2 \quad (\text{S3})$$

$$H_J = -\frac{E_J}{2} \sum_n (|n\rangle \langle n+1| + |n+1\rangle \langle n|) \quad (\text{S4})$$

where $E_C = e^2/2C_\Sigma$ is the electrostatic charging energy to add a single electron to the island with total capaci-

tance C_Σ , \hat{N} is the number operator (number of Cooper pairs), $E_J = I_c \phi_0/(2\pi)$ is the Josephson energy where I_c is the critical current of the Josephson junction, ϕ_0 is the flux quantum, and n is the difference in the number of Cooper pairs across the junction.

To solve for the eigenstates, we use a truncated charge basis where $n = -40, -39, \dots, 0, \dots, 39, 40$:

$$H_T = \begin{pmatrix} 4E_C(-40 - n_g) & -E_J/2 & 0 & \dots & 0 \\ -E_J/2 & 4E_C(-39 - n_g) & -E_J/2 & \dots & 0 \\ \vdots & \vdots & \ddots & \dots & \vdots \\ 0 & 0 & \dots & 4E_C(39 - n_g) & -E_J/2 \\ 0 & 0 & \dots & -E_J/2 & 4E_C(40 - n_g) \end{pmatrix} \quad (\text{S5})$$

with fitting parameters E_C and E_J . The calculated eigenenergies of the lowest five states match our measured results well. We extract $E_C \simeq 198.8$ MHz, $E_J \simeq 11.67$ GHz. The first three transition frequencies of our transmon device and the analogous simulation results are listed in Table S2.

Next, we derive the lowering and raising operators c, c^\dagger in the transmon eigenstate basis. The Cooper-pair number operator in the same truncated charge basis is given by

$$\hat{N} = \begin{pmatrix} -40 & 0 & 0 & \dots & 0 \\ 0 & -39 & 0 & \dots & 0 \\ \vdots & \vdots & \ddots & \dots & \vdots \\ 0 & 0 & \dots & 39 & 0 \\ 0 & 0 & \dots & 0 & 40 \end{pmatrix}. \quad (\text{S6})$$

Thus, the matrix elements of \hat{N} in the transmon eigenbasis can be calculated as $\langle i | \hat{N} | j \rangle$. Below we write \hat{N} in the truncated eigenbasis ($N = 4$) of the transmon. Each matrix element is normalized to the $\hat{N}_4^{0,1}$ matrix element.

$$\hat{N}_4 = \begin{pmatrix} 0.0 & 1.0 & 0.0 & -0.033 \\ 1.0 & 0.0 & -1.374 & 0.0 \\ 0.0 & -1.374 & 0.0 & 1.626 \\ -0.033 & 0.0 & 1.626 & 0.0 \end{pmatrix} \quad (\text{S7})$$

where we can define the lowering and raising operators

c, c^\dagger for the specific transmon device:

$$c = \begin{pmatrix} 0.0 & 1.0 & 0.0 & -0.033 \\ 0.0 & 0.0 & -1.374 & 0.0 \\ 0.0 & 0.0 & 0.0 & 1.626 \\ 0.0 & 0.0 & 0.0 & 0.0 \end{pmatrix}, \quad (\text{S8})$$

$$c^\dagger = \begin{pmatrix} 0.0 & 0.0 & 0.0 & 0.0 \\ 1.0 & 0.0 & 0.0 & 0.0 \\ 0.0 & -1.374 & 0.0 & 0.0 \\ -0.033 & 0.0 & 1.628 & 0.0 \end{pmatrix}. \quad (\text{S9})$$

Experimental setup

Figure 1 of the main text shows a schematic of the experimental setup. The drive signal travels down the coaxial cable and is attenuated and filtered before interacting with the qubit. Bandpass filters at the signal input line reduce both low frequency (<1 GHz) and high frequency (>12 GHz) noise. Homemade Eccosorb CR-110 filters are installed at both input and output ports of the three-dimensional (3D) cavity to reduce infrared radiation entering the cavity. The coaxial cabling and signal line components impose frequency-dependent attenuation. Additionally, the 3D cavity itself functions as a narrow bandpass filter. From the perspective of the qubit, the entire measurement chain can be viewed as a spectral filter on the control signal. In order to faithfully apply the intended control signals, precise knowledge of the frequency-dependent attenuation is required.

TABLE S2. Measured and simulated transmon transition frequencies (GHz)

	$ 0\rangle \rightarrow 1\rangle$	$ 1\rangle \rightarrow 2\rangle$	$ 2\rangle \rightarrow 3\rangle$
Measured	4.09948	3.87409	3.6193
Simulation	4.09948	3.87409	3.6242

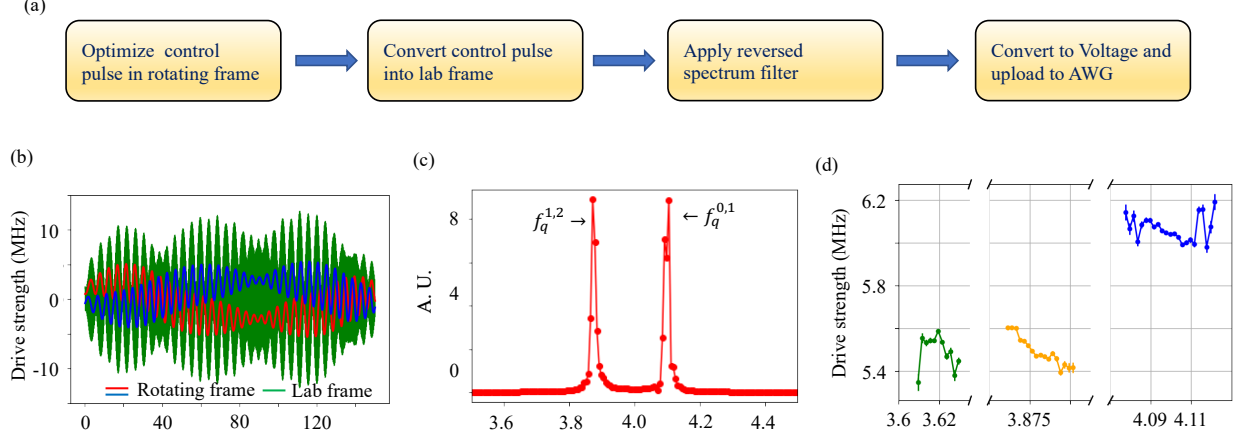


FIG. S2. **Spectrum filter calibration procedure** (a) Flow chart of the main steps required to compensate for frequency-dependent filtering of the measurement chain. (b) Calculated control pulse of the $0 \leftrightarrow 2$ SWAP gate. The slowly varying traces are the real and imaginary component of the control pulse in the rotating frame. The rapidly oscillating trace is the control pulse in laboratory frame. (c) Fast Fourier Transform of the control functions in the laboratory frame. (d) Drive strength with fixed drive amplitude as a function of the drive frequency.

Spectrum filter calibration

In order to calibrate the precise signal amplitude arriving at the qudit, we perform the steps depicted in Fig. S2(a). Starting from the optimized control waveforms in the rotating frame, we convert them into a single waveform in the laboratory frame. Next, we Fourier transform the time-domain control waveform into the frequency domain. There are two main peaks in the frequency domain, each corresponding to one of the qudit transitions as labeled in Fig. S2(c). Because the state $|3\rangle$ is forbidden from occupation during the optimization of the control pulse (through an explicit penalty in the objective function), there is no frequency component related to the $|2\rangle - |3\rangle$ transition.

We adjust the control pulse amplitude for each frequency component according to Fig. S2(d), compensating for the filtering imposed by the measurement chain. Figure S2(d) shows the drive strength for a fixed output amplitude from the arbitrary waveform generator (AWG) as a function of drive frequency. Overall, the drive is attenuated more as the drive frequency decreases. Within a small range of frequency near each qudit transition, the attenuation of the drive is highly nonlinear. Based on the Fourier transform of the control pulse, the frequency components are close to zero everywhere except near the qudit transition frequencies. Therefore, we only measure attenuation of the drive at frequencies near each of the state transitions and linearly interpolate the attenuation elsewhere.

To calculate the attenuation, we apply a cosine waveform with fixed amplitude at frequencies near each qudit transition to induce Rabi oscillations in the time domain.

The Rabi oscillation frequency depends on both the detuning of the drive frequency from each qudit transition as well as the drive strength at that particular frequency. For the case of a two-level system, there are analytical solutions of the state probabilities [43] as a function of time:

$$P_0(t) = \frac{\mathcal{V}_{01}^2}{\Omega_R^2} \cos^2(\Omega_R t/2) \quad (\text{S10})$$

$$P_1(t) = \frac{\mathcal{V}_{01}^2}{\Omega_R^2} \sin^2(\Omega_R t/2) \quad (\text{S11})$$

$$\Omega_R = \sqrt{\mathcal{V}_{01}^2 + \Delta^2} \quad (\text{S12})$$

$$\mathcal{V}_{01} = \langle 0 | \hat{V} | 1 \rangle \quad (\text{S13})$$

where \hat{V} is the drive strength, \mathcal{V}_{01} is the coupling strength between the two states being driven, and Δ is the detuning of the drive from the state transition. P_0, P_1 are population of the two states, and they oscillate with rate Ω_R related to \mathcal{V}_{01} and Δ according to Eq. S12.

Although we have more than two states, the drive frequency is far detuned from other state transitions and this set of solutions is applicable. Furthermore, we ensure that the drive strength is sufficiently small so as not to induce significant two-photon absorption. Because we are using fixed amplitude,

$$\hat{V} = \xi_0 (c + c^\dagger). \quad (\text{S14})$$

We obtain a relationship between $\mathcal{V}_{12}, \mathcal{V}_{23}$ and \mathcal{V}_{01} . Based on the exact form of c, c^\dagger , we have:

$$\mathcal{V}_{12} = 1.374 \cdot \mathcal{V}_{01} \quad (\text{S15})$$

$$\mathcal{V}_{23} = 1.626 \cdot \mathcal{V}_{01}. \quad (\text{S16})$$

Figure S2(d) shows the extracted drive strength in MHz. To compensate for this effect, we rescale the drive strength at $\omega_q^{(0,1)}$ and apply the inverse of the relative attenuation factor to all of the frequency components of the pulse.

In the end, the control waveform is calculated units of Rabi strength (MHz) and must be converted to voltage and uploaded to the AWG for waveform generation. The conversion from MHz to V is determined by driving at a frequency $\omega_d = \omega_q^{0,1}$ at 250 mV on the AWG and observing the Rabi strength to be 6.042 MHz. Therefore, we obtain the conversion factor from MHz to V to be 0.0414 V/MHz.

SIMULATION RESULTS OF THE REPEATED-GATE MEASUREMENT

Figure S3 shows the QuTiP master equation simulation results of the ideal gate with typical values of T_1 and T_2 . The gate is repeated up to 21 times. The simulation qualitatively agrees with our measurement results, see Fig. 2(a)–(d) in the main text.

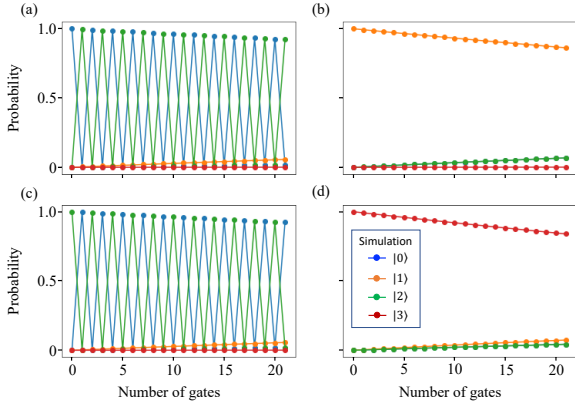


FIG. S3. **Simulation of ideal gate with realistic device decay and decoherence parameters (a)–(d)** The qudit is initialized in $|0\rangle, |1\rangle, |2\rangle, |3\rangle$, respectively.

Estimating the process matrix

A quantum operation is a linear map $\rho \rightarrow \mathcal{E}(\rho)$ which completely describes the dynamics of a quantum system. It is convenient to describe $\mathcal{E}(\rho)$ using a fixed set of operators B_i which form a basis for the quantum operation

on the same state space.

$$\mathcal{E}(\rho) = \sum_{m,n=0}^{d^2-1} \chi_{mn} B_m \rho B_n^\dagger \quad (\text{S17})$$

$$B_i = \{I, Z_\pi^{01}, Z_\pi^{12}, X_\pi^{01}, X_\pi^{12}, Y_\pi^{01}, Y_\pi^{12}, X_\pi^{01} X_\pi^{12}, X_\pi^{12} X_\pi^{01}\} \quad (\text{S18})$$

where χ is a positive Hermitian matrix and depends on the specific gate basis B_i which is not unique. The completeness relation is enforced by

$$\sum_{m,n=0}^{d^2-1} \chi_{mn} B_m^\dagger B_n = I. \quad (\text{S19})$$

We now describe the procedures to estimate χ with the chosen B_i through our repeated-gate results described in the main text. We first write the process matrix in a Cholesky decomposition to ensure that χ is Hermitian:

$$\chi([t]) = L^\dagger([t]) L([t]) \quad (\text{S20})$$

where L is a lower-triangular matrix parameterized by a list of variable $[t]$:

$$L([t]) = \begin{bmatrix} t_0 & 0 & 0 & \cdots & 0 \\ t_1 & t_2 & 0 & \cdots & 0 \\ t_3 & t_4 & t_5 & \cdots & 0 \\ \vdots & \vdots & \vdots & \ddots & \vdots \\ t_{36} & t_{37} & t_{38} & \cdots & t_{44} \end{bmatrix} + i \begin{bmatrix} 0 & 0 & 0 & \cdots & 0 \\ t_{45} & 0 & 0 & \cdots & 0 \\ t_{46} & t_{47} & 0 & \cdots & 0 \\ \vdots & \vdots & \vdots & \ddots & \vdots \\ t_{72} & t_{73} & t_{74} & \cdots & t_{80} \end{bmatrix}. \quad (\text{S21})$$

Next, we apply the mapping defined in Eq. S17 to the initial states $|0\rangle, |1\rangle, |2\rangle$ repeatedly up to 21 times to generate a list of $\rho_n^{0,1,2}$. We compare our measured state occupation probabilities after each gate application to the diagonal elements of each $\rho_n^{0,1,2}$. We fit for the $[t]$ that minimizes the objective function:

$$f([t]) = \sum_{i,k=0}^2 \sum_{n=1}^{21} [m_{i,k,n} - \rho_{n,kk}^i]^2 \quad (\text{S22})$$

where i indicates the initial states, n represents the number of gate applications, and kk represents the diagonal elements of each density matrix. Minimizing an objective function with 81 variables is very computationally expensive. Additionally, there may be many local minima in the relevant parameter space. Because our single gate application result agrees well with our simulation, we believe that the actual process is very close to the target operator. We extract the $[t]$ that corresponds to the U_{targ} and use this $[t]$ as the initial guess to minimize the objective function. To satisfy the completeness relation, we add the constrain given by Eq. S19 to the minimization problem. We use the minimize function from the

scipy.optimize python module (using method ‘SLSQP’). Later, we plot the simulated state probability using the estimate χ alongside measurement results for comparison.

To measure how closely the quantum dynamics approximates the target dynamics, we calculate the entanglement and gate fidelity defined in Eqs. 8–9 in the main text. We generate 1000 random states ρ and calculate the entanglement fidelity for each one. A distribution of the entanglement fidelity is plotted in Fig. S4(a) from which we obtain an average fidelity of 99.2%. To estimate the averaged gate fidelity, we generate gate fidelity distribution for 1000 random state vectors $|\psi\rangle$. Results are shown in Fig. S4(b), from which we acquire averaged

gate fidelity of 99.4%.

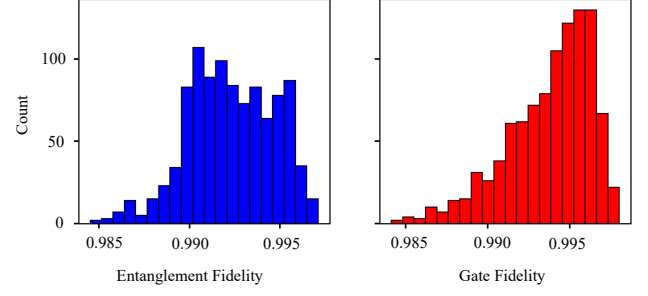


FIG. S4. **Distributions of fidelities** (a) Entanglement fidelity (b) Gate fidelity